Chapter 4

Thermal Equation of State of $(Mg_{0.06}Fe_{0.94})O$

4.1 Introduction

In the previous two chapters, we carried out nuclear resonant spectroscopy and X-ray diffraction on iron-rich (Mg,Fe)O at 300 K and reported properties as a function of pressure and composition. In this chapter, we explore this material in yet another dimension, temperature, measuring the equation of state of $(Mg_{0.06}Fe_{0.94})O$ at high pressures and temperatures. This study will allow us to explore the phase diagram and density of iron-rich (Mg,Fe)O at pressures and temperatures approaching those of Earth's core-mantle boundary region.

4.2 Previous Studies

Previous pressure-volume-temperature ($P-V-T$) studies have shown that the MgO-FeO solid solution is complicated by the existence of phase transitions, a spin transition, and defect clustering as a function of FeO component. The MgO endmember is known to be cubic even beyond the pressure and temperature conditions of the earth's mantle (*Duffy and Ahrens*, 1993). The FeO endmember is thought to be cubic at the pressures and temperatures of the interior of the earth, but at lower temperatures is found to transform to rhombohedral structure at moderate pressures (*Shu et al.*, 1998a, e.g.) and then to the $B8$ NiAs structure at higher pressures (*Fei and Mao*, 1994;

Fischer et al., 2011b, e.g.).

Iron-rich (Mg,Fe)O undergoes a cubic to rhombohedral phase transition at 8-40 GPa, with a phase transition pressure sensitive to both composition and hydrostaticity (Figure 3.1). Studies of the bulk modulus at 0 GPa as a function of composition show differing trends due to sample stoichiometry. Studies of non-stoichiometric, iron-rich (Mg,Fe)O show that both K_S and K_T decreases as a function of Fe concentration (*Jacobsen et al.*, 2002; *Richet et al.*, 1989), where K_S is determined from direct measurements of volume, composition, and of V_P and V_S using ultrasonic interferometry, and K_T is determined in a $P-V$ compression study. The trend is opposite for stoichiometric samples, where ultrasonic interferometry studies for iron-poor samples display a positive trend of K_S with increasing iron content (*Jacobsen et al.*, 2002). In the iron endmember, K_T does indeed depend on stoichiometry, with $Fe_{0.99}O$ being much less compressible than $Fe_{<0.98}O$ (*Zhang*, 2000).

Thermal expansion, $\alpha = \frac{1}{V}(\frac{\delta V}{\delta T})_P$ has been shown to be insensitive to Fe content for Mg-containing ferropericlase (*Zhang and Kostak Jr*, 2002). Yet, it appears to be sensitive to defect concentration. In the Fe end member, α is about 30% larger for $Fe_{0.942}O$ than $Fe_{0.987}O$ (*Zhang and Zhao*, 2005). In this study, we aim to measure the $P-V-T$ equation of state $(Mg_{0.06}Fe_{0.94})O$, first to constrain the thermoelasticity of iron-rich (Mg,Fe)O and second to see if these trends apply to the equation of state of iron-rich (Mg,Fe)O.

4.3 Experimental Details

Two experiments were conducted in this study. For the unbuffered experiment, a symmetric diamond anvil cell with 300 μm-culet diamonds was prepared. $(Mg_{0.06}Fe_{0.94})O$ was lightly ground with NaCl powder (1:1 by volume) in an agate mortar under ethanol, allowed to dry, then pressed into a pellet. This mixture was loaded between two thin NaCl plates (<10 μm), and the remaining space in the rhenium gasket sample chamber was filled with neon using the COMPRES/GSECARS gas-loading system (*Rivers et al.*, 2008). To keep the NaCl dehydrated, the pellet was consistently stored in a desiccator when not in use, and the loaded diamond anvil was placed under vacuum for about one hour and purged with argon before being put into the gas-loading system. In a second high

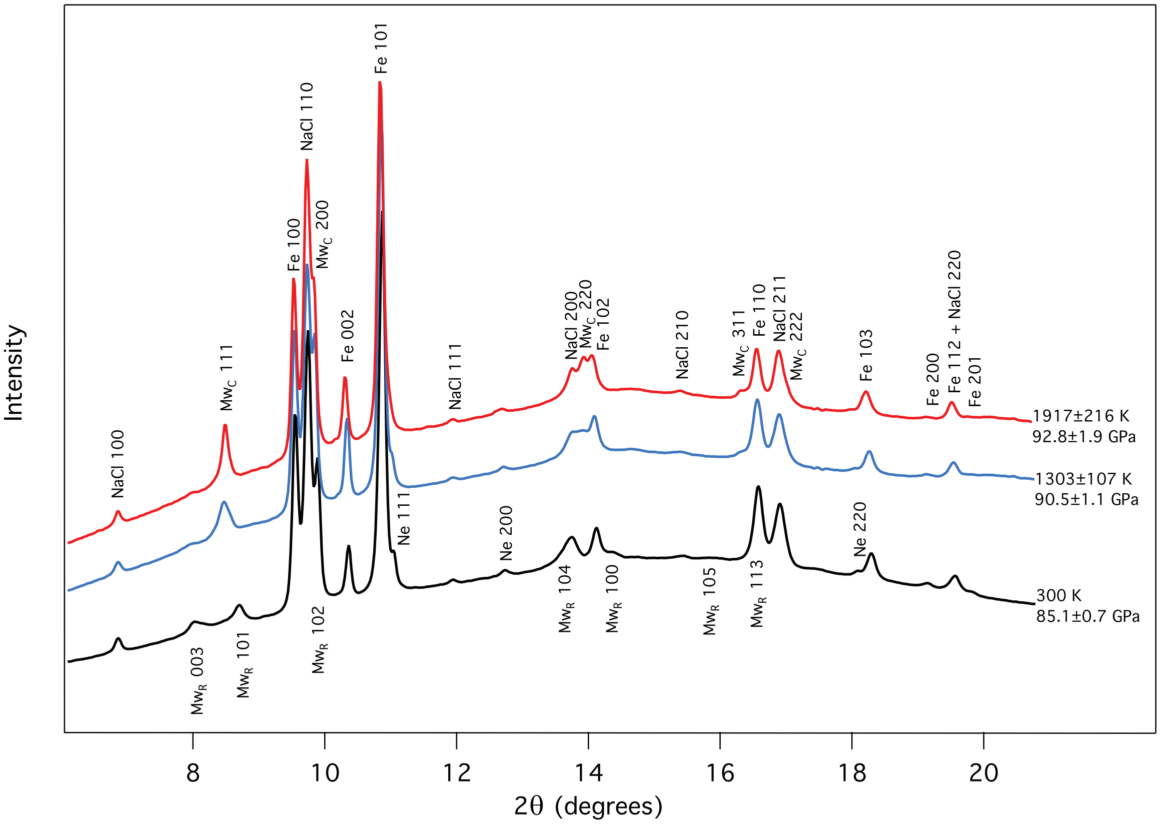

Figure 4.1: Example XRD spectra at 85 GPa showing peak identifications for *B*2-NaCl, *hcp*-Fe, and Ne. ($Mg_{0.06}Fe_{0.94}$)O is rhombohedral at room temperature (Mw$_R$, *R-3m*) and cubic at high temperature (Mw$_C$, *Fm-3m*). Pressures listed were determined by the equation of state of *hcp*-Fe (*Dewaele et al.*, 2006; *Murphy et al.*, 2011)

pressure experiment, 250 μm-culet diamonds were used. Otherwise, the preparation differed in that the sample pellet also included a Fe metal (1:1 Mw94:Fe by weight) as an in-situ oxygen buffer and pressure marker.

The high temperature powder diffraction experiments were conducted at the 13-ID-D beamline (GSECARS) at the Advanced Photon Source, Argonne National Laboratory. High temperatures were achieved in-situ by laser heating from both sides with a split infrared fiber laser (*Prakapenka et al.*, 2008) with temperature determined spectroradiametrically on both up and downstream sides (e.g. *Heinz and Jeanloz*, 1987). Using an incident X-ray beam of $\lambda = 0.3344$ Å, angle-dispersive X-ray diffraction patterns were recorded onto a MAR165 CCD detector and subsequently integrated using Fit2D (*Hammersley et al.*, 1996). Example spectra are shown in Figure 4.1.

The 2θ angles corresponding to lattice reflections of $(Mg_{0.06}Fe_{0.94})O$, NaCl, Fe, and Ne were determined by fitting the spectra with Voigt peaks using Igor Pro (WaveMetrics, Lake Oswego, OR, USA). Unit cell volumes were determined using unweighted linear regression using the *Unit Cell* refinement software package (*Holland and Redfern*, 1997), which assumes a minimum uncertainty of 0.005 degrees on each lattice reflection, with errors on the unit cell weighted by goodness of fit. The $B2$-NaCl thermal equation of state of *Fei et al.* (2007b) was used to determine pressure in the unbuffered experiment, and to compare that dataset to the buffered experiment. Pressures in the second experiment were determined using the unit cell volume of *hcp*-iron. We used the Fe equation of state given by *Dewaele et al.* (2006) for the data collected at 300 K, and the quasiharmonic thermal pressure given by *Murphy et al.* (2011). The difference between the two pressure scales is small, with a resulting pressure increase of 0.01 to 0.4 GPa for the *Murphy et al.* (2011) values.

To determine temperature and error of our measurements, we took the average and standard deviation of multiple temperature measurements, which are known to have a precision of 100 K (*Shen et al.*, 2001). Errors in temperature and unit cell of NaCl and *hcp*-Fe were propagated into error in pressure assuming a Gaussian distribution of errors in a simple Monte Carlo error propagation. In the buffered experiment, the discrepancy between measured upstream and downstream temperatures, and the sharp diffraction peaks that show there is no temperature gradient, made it clear that we could not assume a Gaussian distribution. In order to not place undo constraints on the supposed temperature distribution, we used a flat distribution in the error propagation. Calculated volumes and pressures of the buffered dataset are presented in Table 4.1. Calculated volumes and pressures of the unbuffered dataset are presented in Table 4.2.

4.4 Results

4.4.1 Phase Identification

In the P–T range of study, we identified cubic (Mg,Fe)O at high temperature and rhombohedral or a mixture of rhombohedral and cubic (Mg,Fe)O at room temperature. We interpret the mixture to be

Table 4.1: Pressure-volume-temperature data for the buffered experiment. ^{a}Pressure was determined by the equation of state of *hcp*-Fe from *Dewaele et al.* (2006) and *Murphy et al.* (2011).

Pressure^a (GPa)	Temperature (K)	Vol$_{Mw94}$ (Å^3)	Vol$_{NaCl}$ (Å^3)	Vol$_{Fe}$ (Å^3)
116.5(7)	1056(13)	6.94(3)	20.10(2)	16.50(2)
118(1)	1218(85)	6.94(2)	20.13(3)	16.50(2)
118.0(9)	1295(124)	6.95(2)	20.11(2)	16.51(2)
119(1)	1436(191)	6.95(2)	20.12(3)	16.53(2)
120(2)	1649(278)	6.95(2)	20.11(2)	16.55(2)
102.5(4)	1124(29)	7.17(1)	20.86(2)	16.90(1)
103.0(4)	1212(15)	7.17(2)	20.87(2)	16.90(1)
103.8(4)	1370(36)	7.19(2)	20.89(2)	16.92(1)
104.8(6)	1563(108)	7.19(1)	20.89(2)	16.94(1)
105.5(6)	1646(109)	7.19(2)	20.89(2)	16.94(1)
106.4(9)	1852(166)	7.20(2)	20.90(2)	16.97(1)
95.0(5)	1184(61)	7.26(3)	21.5(1)	17.13(1)
95.3(7)	1296(139)	7.29(1)	21.45(9)	17.16(1)
96(1)	1426(193)	7.30(2)	21.5(1)	17.18(1)
97(1)	1620(228)	7.34(1)	21.5(1)	17.19(1)
90.2(6)	1201(111)	7.40(2)	21.66(2)	17.29(1)
90.5(6)	1303(107)	7.43(2)	21.68(2)	17.31(1)
91.2(7)	1459(130)	7.43(3)	21.68(2)	17.33(1)
93(1)	1707(204)	7.45(2)	21.69(2)	17.36(1)
93(1)	1807(246)	7.45(2)	21.70(2)	17.37(1)
93(1)	1917(216)	7.43(1)	21.71(2)	17.40(1)
84.5(7)	1105(119)	7.52(3)	21.98(4)	17.45(1)
84.4(8)	1162(144)	7.52(3)	22.00(3)	17.48(2)
84.7(8)	1270(152)	7.52(2)	22.00(3)	17.50(1)
85(1)	1379(193)	7.54(3)	21.98(2)	17.52(1)
77.3(6)	1051(64)	7.65(2)	22.44(3)	17.70(2)
77.5(8)	1135(130)	7.66(2)	22.45(3)	17.71(2)
79(1)	1332(193)	7.66(2)	22.45(3)	17.73(2)
79(1)	1460(260)	7.66(1)	22.47(3)	17.75(2)
75.7(7)	1089(145)	7.70(1)	22.69(2)	17.77(1)
76(1)	1169(211)	7.71(1)	22.65(2)	17.78(1)
77(1)	1285(247)	7.72(1)	22.67(2)	17.79(1)
77(1)	1356(298)	7.72(1)	22.66(3)	17.80(1)
77(2)	1490(346)	7.74(1)	22.67(3)	17.83(1)
72.4(8)	1119(155)	7.80(2)	23.00(3)	17.90(1)
73(1)	1179(211)	7.81(2)	23.02(3)	17.91(1)
73(1)	1268(275)	7.81(3)	23.05(4)	17.92(1)
74(1)	1454(277)	7.81(2)	23.04(3)	17.94(1)
75(2)	1626(359)	7.81(2)	23.06(2)	17.97(1)
75(2)	1604(350)	7.81(1)	23.03(3)	17.97(1)
60.1(8)	1131(128)	8.05(2)	24.02(7)	18.41(2)
60.4(8)	1205(156)	8.05(2)	24.03(6)	18.42(2)
61(1)	1364(189)	8.06(2)	24.01(4)	18.45(2)
62(1)	1520(265)	8.06(2)	24.04(4)	18.47(1)
63(1)	1671(308)	8.07(2)	24.06(4)	18.50(1)
53.9(7)	1136(100)	8.21(1)	24.74(5)	18.70(3)
54.2(9)	1205(141)	8.22(1)	24.74(6)	18.71(3)
55(1)	1356(247)	8.22(1)	24.72(7)	18.72(3)
56(1)	1466(255)	8.23(1)	24.76(6)	18.74(2)
56(1)	1558(291)	8.23(1)	24.75(6)	18.75(2)
57(1)	1631(308)	8.23(1)	24.77(7)	18.76(2)
51(1)	1311(245)	8.33(1)	25.29(4)	18.94(2)
50.0(8)	1177(164)	8.32(1)	25.27(4)	18.91(2)
51(2)	1435(328)	8.34(1)	25.31(3)	18.95(2)
38.4(4)	1324(51)	8.69(1)	27.07(7)	19.63(2)
38.7(6)	1370(76)	8.69(1)	27.12(4)	19.63(3)
39.0(7)	1416(122)	8.70(1)	27.11(6)	19.64(3)
40(1)	1581(246)	8.72(1)	27.15(6)	19.65(3)
40(1)	1643(294)	8.72(1)	27.13(7)	19.66(2)
33.1(4)	300	8.58(3)	26.99(5)	19.50(2)

Table 4.2: Pressure-volume-temperature data for the unbuffered experiment. ^{a}Pressure was determined from the equation of state of $B2$-NaCl (*Fei et al.*, 2007b).

Pressure^a (GPa)	Temperature (K)	Vol$_{Mw94}$ ($\AA^3$)	Vol$_{NaCl}$ ($\AA^3$)	Pressure^a (GPa)	Temperature (K)	Vol$_{Mw94}$ ($\AA^3$)	Vol$_{NaCl}$ ($\AA^3$)
71.5(4)	1227(11)	7.77(2)	22.84(3)	55(1)	1396(42)	8.22(3)	24.6(1)
71.7(6)	1312(14)	7.78(2)	22.85(5)	55(1)	1579(16)	8.23(2)	24.6(1)
72.0(5)	1442(28)	7.79(2)	22.88(4)	56(1)	1670(24)	8.23(1)	24.6(1)
71.4(4)	1208(23)	7.77(2)	22.85(3)	56(1)	1731(9)	8.24(1)	24.6(1)
71.7(5)	1317(27)	7.78(2)	22.86(4)	51.9(5)	300	8.09(5)	24.37(6)
71.9(4)	1413(26)	7.78(2)	22.88(4)	54.4(8)	1140(21)	8.15(8)	24.49(8)
70(1)	1192(44)	7.85(5)	22.99(8)	54.7(6)	1239(6)	8.16(6)	24.51(7)
70.0(9)	1306(62)	7.84(3)	23.00(5)	55.4(6)	1437(16)	8.18(3)	24.52(6)
70.5(7)	1433(19)	7.85(1)	23.01(5)	55.3(8)	1483(53)	8.22(1)	24.56(6)
69.9(7)	1173(15)	7.82(3)	22.96(6)	51.9(1)	300	8.06(3)	24.37(1)
70.1(7)	1279(36)	7.83(3)	22.98(4)	47(1)	1195(20)	8.39(4)	25.5(2)
70.5(9)	1396(49)	7.85(3)	22.99(6)	48(1)	1398(34)	8.4(3)	25.5(1)
67.4(9)	1226(28)	7.89(6)	23.21(7)	48.2(9)	1591(24)	8.41(2)	25.5(1)
67.7(7)	1293(17)	7.89(5)	23.21(6)	48.8(9)	1760(26)	8.42(1)	25.51(1)
68.0(6)	1403(20)	7.9(5)	23.22(5)	44.6(7)	300	8.24(3)	25.25(9)
64.9(6)	300	7.77(1)	23.06(5)	45(1)	1248(24)	8.42(5)	25.7(2)
67.4(6)	1180(23)	7.88(5)	23.18(5)	46(1)	1429(15)	8.42(4)	25.7(2)
67.8(5)	1306(7)	7.89(5)	23.20(5)	46(1)	1613(15)	8.44(3)	25.8(2)
67.9(6)	1351(15)	7.89(5)	23.21(5)	47(1)	1705(35)	8.45(2)	25.8(1)
68.1(6)	1420(16)	7.9(4)	23.22(5)	42.5(8)	300	8.34(4)	25.54(1)
63.3(3)	1216(7)	7.96(4)	23.58(2)	41(1)	1186(32)	8.55(2)	26.2(2)
63.6(2)	1295(2)	7.97(4)	23.59(2)	42.0(9)	1387(6)	8.56(2)	26.3(1)
64.1(4)	1412(17)	7.97(3)	23.60(3)	43(1)	1561(33)	8.57(2)	26.3(1)
63.6(2)	1212(10)	7.95(3)	23.55(1)	42.8(8)	1584(12)	8.57(2)	26.3(1)
63.8(3)	1289(11)	7.96(3)	23.57(2)	38.9(6)	300	8.4(3)	26.0(1)
64.1(3)	1430(13)	7.97(3)	23.60(3)	35(1)	300	8.55(7)	26.7(2)
60.5(5)	1215(27)	8.05(5)	23.86(4)	39(1)	1265(35)	8.62(4)	26.7(2)
61.1(2)	1335(14)	8.05(4)	23.86(1)	39(1)	1398(37)	8.63(4)	26.7(2)
61.4(3)	1424(15)	8.05(3)	23.87(3)	39(1)	1395(23)	8.63(4)	26.7(2)
58.2(1)	300	7.91(3)	23.70(1)	40(1)	1562(38)	8.65(4)	26.8(1)
60.9(9)	1210(10)	8.08(8)	23.82(9)	40(1)	1613(28)	8.65(4)	26.8(1)
61(1)	1322(17)	8.04(5)	23.84(9)	35.8(6)	300	8.53(9)	26.5(1)
62.1(8)	1446(23)	8.03(1)	23.81(7)	38.4(9)	1165(51)	8.6(3)	26.7(1)
57.6(3)	1203(24)	8.13(4)	24.16(3)	39(1)	1436(45)	8.63(3)	26.7(2)
58.0(5)	1317(40)	8.13(3)	24.18(3)	39.7(9)	1594(17)	8.65(4)	26.8(1)
58.4(4)	1424(43)	8.13(3)	24.19(2)	35.9(6)	300	8.48(1)	26.5(1)
58.3(4)	1390(20)	8.13(3)	24.18(3)	31.4(6)	300	8.63(4)	27.3(1)
55.1(2)	300	7.93(6)	24.02(2)	34.6(9)	1207(77)	8.72(1)	27.4(1)
57.9(4)	1207(36)	8.11(3)	24.13(2)	35.0(9)	1295(68)	8.73(1)	27.4(1)
58.1(3)	1308(12)	8.12(3)	24.16(2)	35.3(8)	1384(50)	8.76(1)	27.4(1)
58.4(2)	1382(19)	8.12(3)	24.16(1)	35.5(7)	1475(25)	8.77(1)	27.4(1)
58.8(6)	1451(37)	8.13(3)	24.16(5)	31.9(4)	300	8.61(2)	27.19(8)
55.2(2)	300	7.98(3)	24.01(2)	29.8(7)	300	8.62(11)	27.6(1)
55.7(3)	1245(22)	8.18(3)	24.39(2)	33(1)	1224(31)	8.76(2)	27.6(2)
56.2(5)	1337(18)	8.18(2)	24.39(4)	33.6(9)	1454(41)	8.79(1)	27.7(1)
56.1(3)	1371(16)	8.18(2)	24.41(3)	34(1)	1630(31)	8.81(1)	27.8(2)
56.1(4)	1386(32)	8.17(2)	24.41(3)	30.1(4)	300	8.66(4)	27.53(8)
53.0(2)	300	8.02(1)	24.24(2)	31.9(9)	1235(36)	8.75(7)	27.9(2)
55.9(6)	1270(23)	8.15(3)	24.38(6)	32(1)	1384(65)	8.78(5)	28.0(2)
56.1(3)	1346(18)	8.16(3)	24.40(2)	32.4(9)	1526(21)	8.82(4)	28.0(2)
56.4(3)	1422(15)	8.17(2)	24.40(3)	32.4(7)	1391(60)	8.79(4)	27.93(9)
53.0(2)	300	8.03(2)	24.24(2)	32.8(5)	1510(31)	8.81(4)	27.95(8)
54(2)	1224(38)	8.21(4)	24.6(2)				

a result of incomplete back-transformation of cubic to rhombohedral phase on quench. We plot our results in Figure 4.2. Our before-heating points are shown in gray, bracketing the room temperature cubic-rhombohedral transition between 13 and 24 GPa. Representative error bars (bottom right) show the discrepancy in average standard deviation of temperature measurements between the two experiments.

The phase identifications presented in Figure 4.2 are consistent with previous results in that there is no observable $B8$-structured ($Mg_{0.06}Fe_{0.94}$)O in the pressure and temperature range studied (*Kondo et al.*, 2004). Our study, however, disagrees with the location of the rhombohedral-cubic phase boundary of iron-rich (Mg,Fe)O at high temperature. Where we find no evidence of rhombohedral ($Mg_{0.06}Fe_{0.94}$)O at the high temperatures explored in our study, *Kondo et al.* (2004) find a transition of cubic to rhombohedral ($Mg_{0.1}Fe_{0.9}$)O and ($Mg_{0.05}Fe_{0.95}$)O at 1100 to 1500 K, 70 to 100 GPa (Figure 4.2).

4.4.2 Equations of State

The buffered and unbuffered datasets were fit to a 3rd-order Birch-Murnaghan equation of state using EOSFIT (*Angel*, 2000), with the following relations:

$$P(V) = 3K_0 f_E (1+2f_E)^{\frac{5}{2}} \left\{ 1 + \frac{3}{4}(K_0' - 4) f_E \right\} \tag{4.1}$$

$$f_E = \frac{1}{2}\left[\left(\frac{V_0}{V}\right)^{\frac{2}{3}} - 1\right] \tag{4.2}$$

$$V_0(T) = V_0(T_0)\exp(\alpha_0(T - T_0)) \tag{4.3}$$

$$K(T) = K_0 + (T - T_0)\left(\frac{\partial K}{\partial T}\right)_P \tag{4.4}$$

where P is pressure in GPa, K_0 is the bulk modulus in GPa at the reference pressure, in our case the isothermal bulk modulus at either 0 or 30 GPa, f_E is Eulerian strain, V and V_0 are volume and initial volume, respectively, in units of Å^3/atom. In the high temperature formulation (Equations

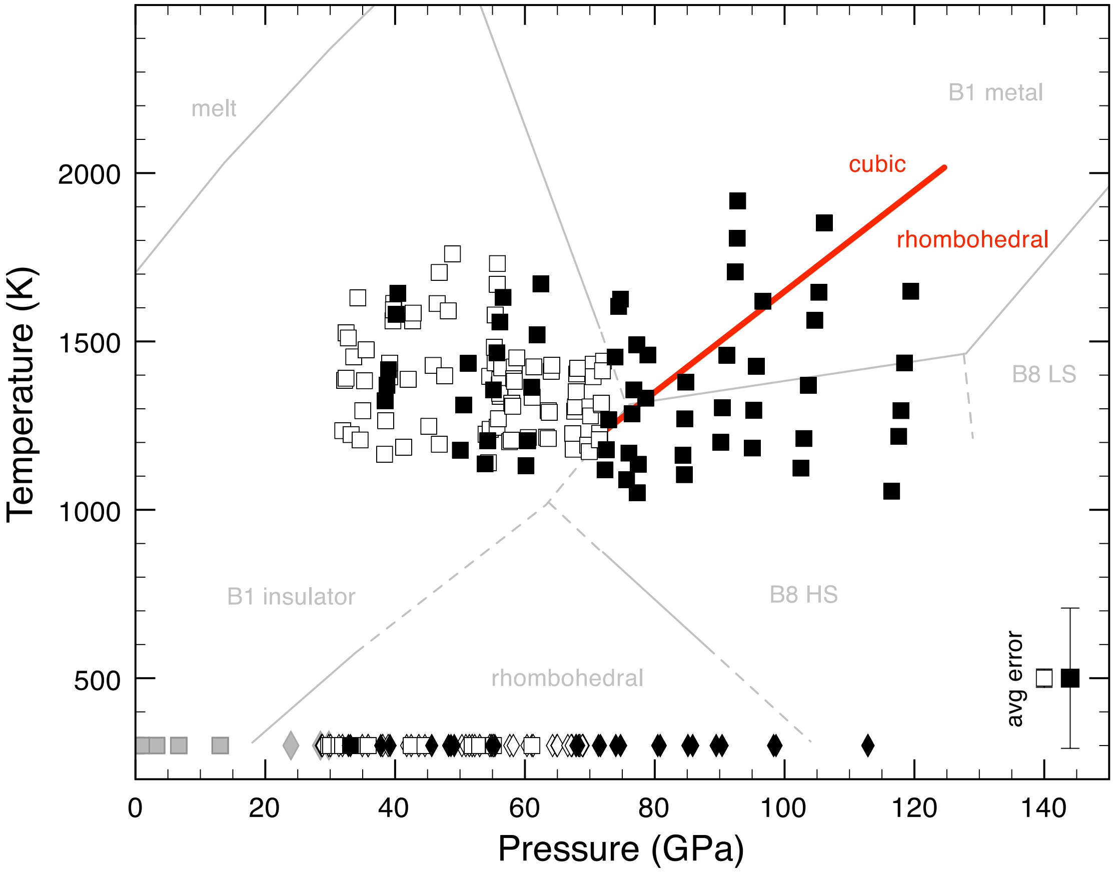

Figure 4.2: Phase identification of $(Mg_{0.06}Fe_{0.94})O$ in P–T space. $(Mg_{0.06}Fe_{0.94})O$ is cubic (unbuffered: white boxes, buffered: black boxes) at high temperature and rhombohedral (unbuffered: white diamonds, buffered: black diamonds) at room temperature, with exception of some quench measurements that contained a mixture of cubic and rhombohedral phases. Before-heating points are shown below 25 GPa in gray. Light gray lines: the latest phase diagram of wüstite (*Fei and Mao*, 1994; *Fischer and Campbell*, 2010; *Fischer et al.*, 2011b,a; *Kondo et al.*, 2004; *Ozawa et al.*, 2010, 2011). Red line: rhombohedral-cubic phase boundary of $(Mg_{0.1}Fe_{0.9})O$ and $(Mg_{0.05}Fe_{0.95})O$ measured by *Kondo et al.* (2004). Representative error bars are also shown in the lower right corner.

Table 4.3: 3rd-order Birch-Murnaghan equation of state parameters for the buffered dataset using *hcp*-Fe as a pressure marker (*Dewaele et al.*, 2006; *Murphy et al.*, 2011). Reference pressure of either 0 or 30 GPa result in equivalent equations of state.

	$P_0 = 0$ GPa	$P_0 = 30$ GPa
V_0 (Å^3)	9.88(9)	8.6(3)
K_{0T} (GPa)	193(14)	275(11)
K'_{0T}	3.0(2)	2.6(2)
$\alpha_0(\times 10^{-5}$ K$^{-1})$	4.2(7)	3.2(4)
$\partial K/\partial T$ (GPa/K)	$-0.017(6)$	$-0.021(7)$

4.3,4.4), T and T_0 are temperature and reference temperature, respectively, in Kelvin, α_0 is the thermal expansion coefficient, in units of K^{-1}, and $\partial K/\partial T$ is the isobaric temperature derivative of the bulk modulus, in units of (GPa/K).

The equation of state of the buffered dataset (32 to 117 GPa) was fit using pressures given by the equation of state of hcp-Fe (*Dewaele et al.*, 2006; *Murphy et al.*, 2011, (Table 4.3)).

The fitted V_0 from our study is 9.89(7) Å^3/atom, when using *hcp*-Fe metal as a pressure indicator, which is consistent with our starting material volume of 9.90(1) Å^3/atom, measured on the sample outside of the diamond anvil cell, which in turn is consistent with our Mössbauer measurement showing that Fe$^{2^+}$ is below detection limit ($< 2\%$). The range of fitted K_0 includes that predicted for nearly stoichiometric (Mg,Fe)O (*Jacobsen et al.*, 2002) .

Figure 4.3 shows the results from this buffered experiment, showing volume as a function of pressure and temperature. Also shown are the volumes measured as we compressed the cell before the heating experiment began. We did not include these points in the fit. The steeper $\partial V/\partial P$ of these points, i.e. lower K_0, is more consistent with (Mg,Fe)O containing >2% vacancies (*Zhang*, 2000; *Jacobsen et al.*, 2002).

Table 4.4 shows the fitting results of both buffered and unbuffered datasets with reference pressures of either $P_0 = 0$ GPa or $P_0 = 30$ GPa, using pressure determined by the equation of state of $B2$-NaCl (*Fei et al.*, 2007b).

The limited pressure range (30 to 70 GPa) of the unbuffered dataset proved difficult to fit without external constraints, so we fixed $\partial K/\partial T$ to that of the buffered dataset. If, instead of fixing V_0 of one dataset to the other, we fix K_0 to 180 GPa, the predicted bulk modulus for a stoichiometric

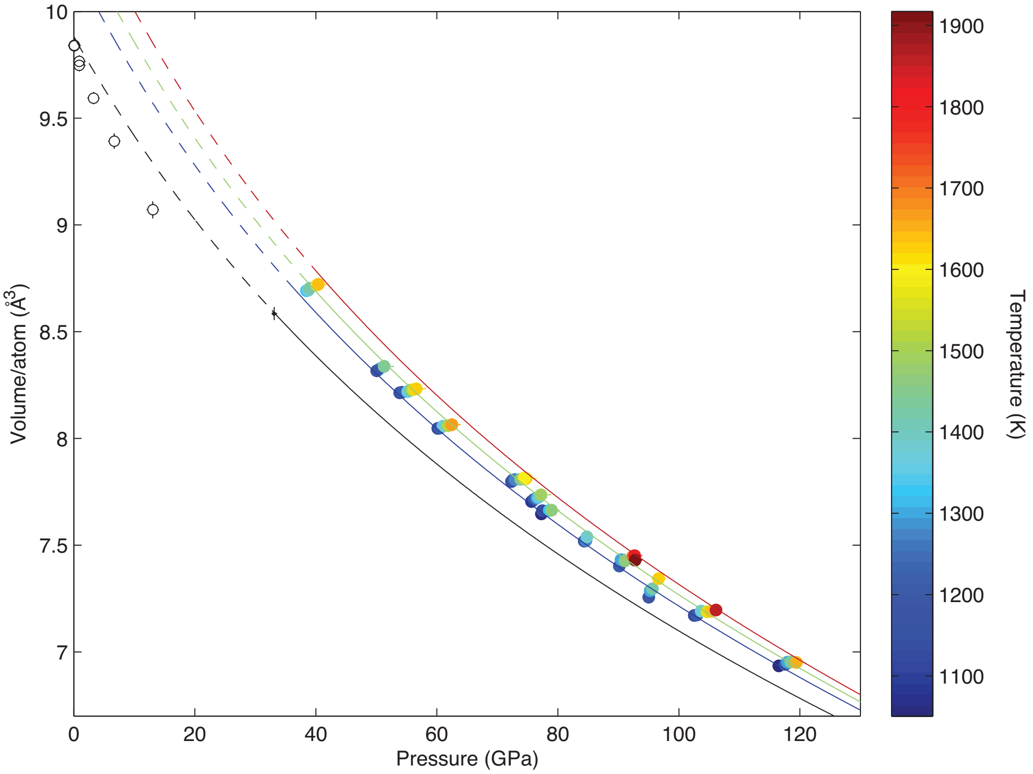

Figure 4.3: $P-V-T$ data and isotherms of $B1$-structured ($Mg_{0.06}Fe_{0.94}$)O in the buffered experiment. Pressures were determined using the equation of state of Fe (*Dewaele et al.*, 2006; *Murphy et al.*, 2011). Open circles: pre-experiment volumes at pressures determined by the equation of state of $B1$-NaCl (JCPDS 5-0628).

Table 4.4: 3rd-order Birch-Murnahan equation of state parameters the both the buffered and unbuffered dataset using $B2$-NaCl as a pressure marker (*Fei et al.*, 2007b). In both cases, the $\partial K/\partial T$ of the unbuffered dataset is fixed to that of the buffered.

	$P_0 = 0$ GPa		$P_0 = 30$ GPa	
	buffered	unbuffered	buffered	unbuffered
V_0 (Å^3)	9.85(8)	9.8(1)	8.69(3)	8.64(1)
K_{0T} (GPa)	202(12)	201(24)	276(9)	283(11)
K'_{0T}	2.7(1)	3.0(4)	2.3(1)	2.6(5)
$\alpha_0(\times 10^{-5}\ \mathrm{K}^{-1})$	3.3(6)	3.6(1)	2.5(4)	2.89(7)
$\partial K/\partial T$ (GPa/K)	$-0.013(5)$	-0.013 (*fixed*)	$-0.016(7)$	-0.016 (*fixed*)

Table 4.5: Equation of state parameters using $B2$-NaCl as a pressure marker (*Fei et al.*, 2007b), where we fix K_{0T} to 180 GPa.

	buffered	unbuffered
V_0 (Å^3)	10.0(3)	9.9(1)
K_{0T} (GPa)	180 (*fixed*)	180 (*fixed*)
K'_{0T}	2.95(7)	3.29(6)
$\alpha_0(\times 10^{-5}\ \mathrm{K}^{-1})$	3.0(7)	3.41(7)
$\partial K/\partial T$ (GPa/K)	$-0.010(5)$	-0.010 (*fixed*)

magnesiowüstite (*Jacobsen et al.*, 2002), we again get equation of state parameters that yield values consistent with our previous fits (Table 4.5).

Figure 4.4 shows the results from the unbuffered experiment, showing volume change of $(Mg_{0.06}Fe_{0.94})O$ as a function of pressure and temperature, using NaCl as a pressure marker (*Fei et al.*, 2007b).

4.5 Discussion

4.5.1 Effect of Buffering on Equation of State

In Figure 4.5, we compare the first dataset to the second, showing example volumes and isotherms at 1200, 1500, and 1800 K. At 50 GPa, the calculated thermal expansion coefficients are $\alpha_{buffered} = 2.1(6) \times 10^{-5}\mathrm{K}^{-1}$ and $\alpha_{unbuffered} = 2.6(1) \times 10^{-5}\mathrm{K}^{-1}$.

We first note that the sole room temperature quench point of the buffered dataset is consistent with the unbuffered dataset (Figure 4.5, black filled circle and squares), and the room temperature equations of state are consistent (Table 4.4). The initial thermal expansion coefficient (α_0) of the two datasets are also consistent within error.

The discrepancy between un-annealed (before heating) low pressure and annealed (heated) high pressure measurements suggests a physical difference between cold-compressed and annealed iron-rich (Mg,Fe)O even without an Fe metal buffer. It has been proposed that vacancy concentrations in non-stoichiometric FeO-bearing samples are reduced with the exsolution of $(Fe,Mg)Fe_2O_4$ at high pressure and temperature according to

$$(Mg_xFe_y)O \rightarrow a(Mg_{x'}Fe_{1-x'})Fe_2O_4 + b(Mg_{x''}Fe_{y''})O \tag{4.5}$$

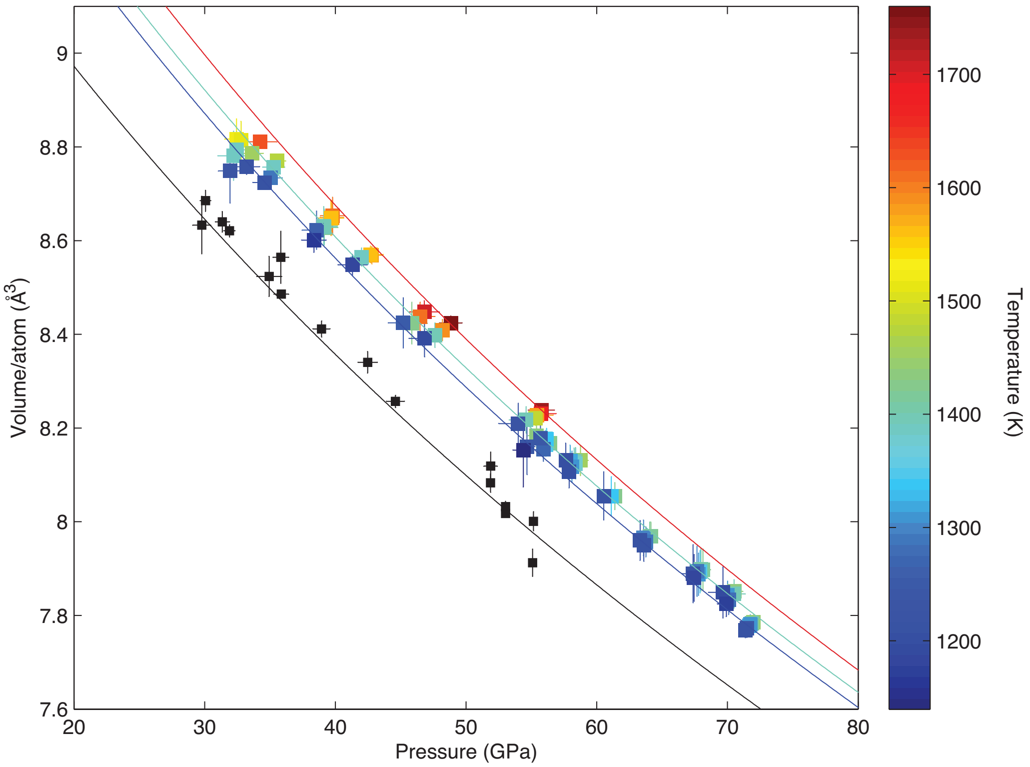

Figure 4.4: $P-V-T$ data and isotherms of $B1$-structured $(\mathrm{Mg}_{0.06}\mathrm{Fe}_{0.94})\mathrm{O}$ in the unbuffered experiment with $\partial K/\partial T$ fixed to that of the buffered experiment. Equation of state parameters corresponding to these curves are those in Table 4.4.

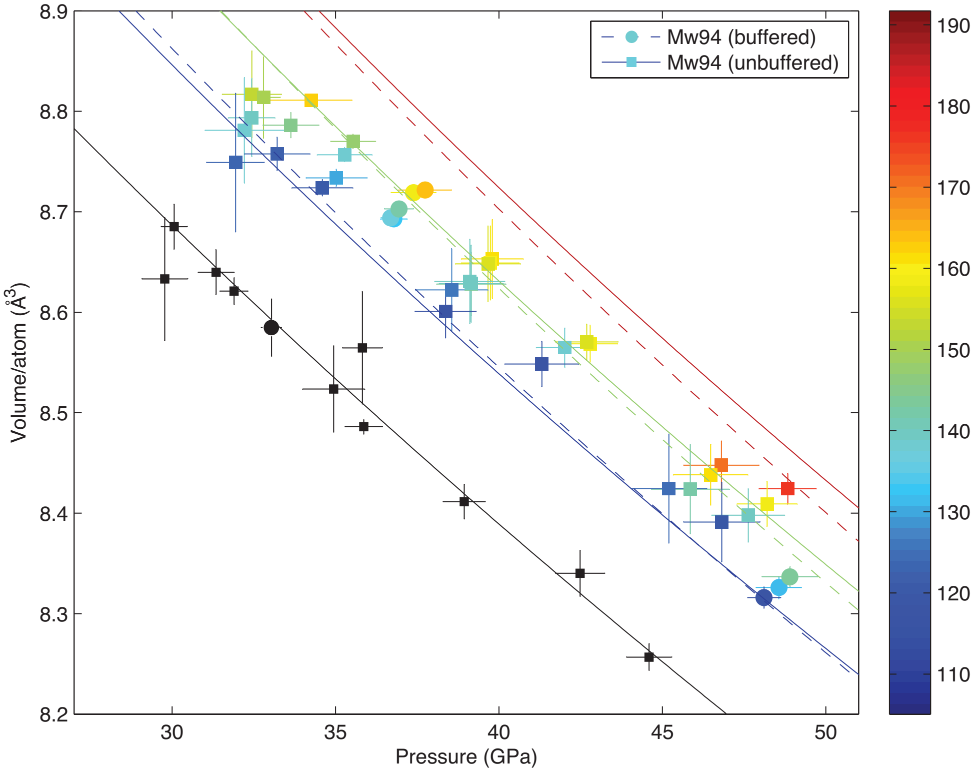

Figure 4.5: Overlay of data and equations of state of $(Mg_{0.06}Fe_{0.94})O$ in both experiments. The unbuffered (squares, solid lines) and buffered (circles, dashed lines) datasets are in good agreement where they overlap in pressure-temperature conditions.

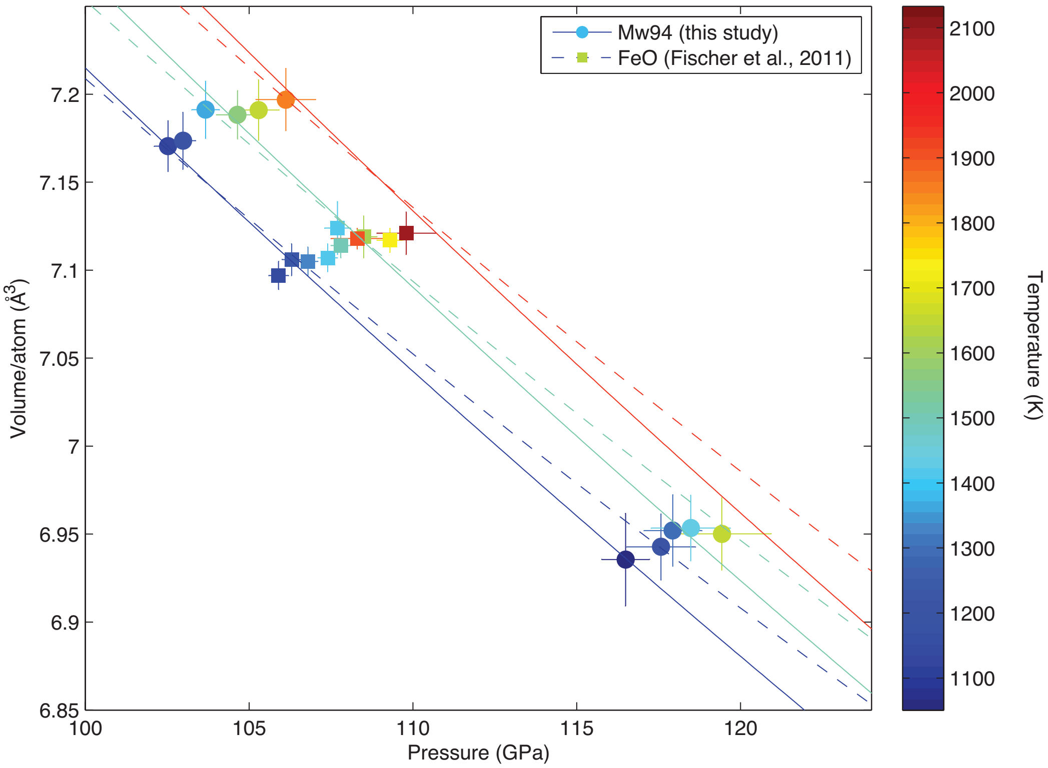

Figure 4.6: Comparison of volume measurements and equations of state of buffered ($Mg_{0.06}Fe_{0.94}$)O (circles, solid lines) to $B1$-FeO (squares, dashed lines) (*Fischer et al.*, 2011b).

where $(x'' + y'') > (x + y)$, ensuring the stoichiometry of the (Mg,Fe)O phase regardless of oxygen fugacity (*Zhang and Zhao*, 2005; *McCammon et al.*, 1998). If this were true in our case, it would also explain the similarity between the buffered and unbuffered datasets at high pressure and temperature.

4.5.2 Effect of Composition on the Thermal Equation of State of (Mg,Fe)O

In Figure 4.6, we compare ($Mg_{0.06}Fe_{0.94}$)O to the equation of state and volumes of FeO (*Fischer et al.*, 2011b) to determine the effect of incorporation of Mg on the equation of state FeO. Both experiments were conducted with in-situ Fe metal buffer/pressure marker. At our highest pressure, 117 GPa, we were not able to discern a difference between the thermal expansion of Mw94 and FeO ($\alpha_{(Mg_{0.06}Fe_{0.94})O} = 1.5(7) \times 10^{-5}$ K^{-1} and $\alpha_{FeO} \approx 1.4(1) \times 10^{-5}$ K^{-1}).

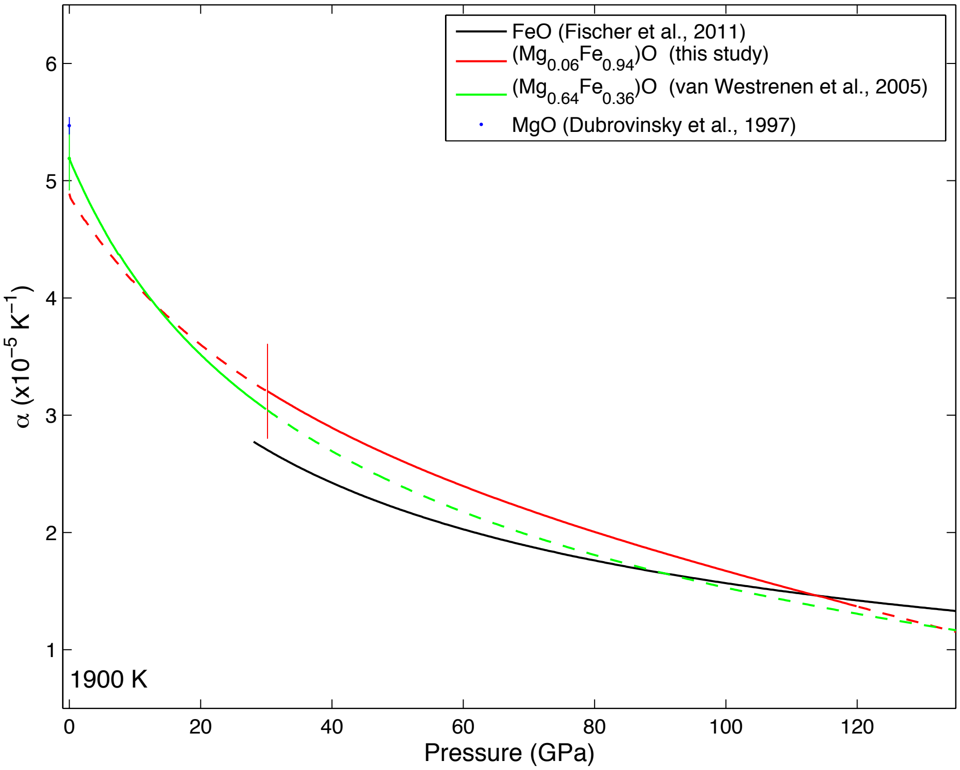

Figure 4.7: Thermal expansion at 1900 K as a function of pressure (Table 4.3), compared to FeO (*Fischer et al.*, 2011b), $(Mg_{0.64}Fe_{0.36})O$ (*Westrenen et al.*, 2005), and MgO (*Dubrovinsky and Saxena*, 1997). Dashed lines show areas of extrapolated curves, and error bars shown are the 1σ error in thermal expansion coefficient.

In Figure 4.7, we plot the thermal expansion of different members of the (Mg,Fe)O solid solution as a function of pressure, at 1900 K. At ambient pressure, the thermal expansion of MgO, $(Mg_{0.64}Fe_{0.36})O$, and FeO vary as a function of composition. Within our experimental uncertainties, we cannot resolve a compositional effect on the thermal expansion of (Mg,Fe)O at high pressures.

Given the different experimental conditions of our buffered and unbuffered datasets, Fe/Mg compositional variation may also be a concern. It is imaginable that buffering with Fe metal could lead to a different Fe/Mg ratio in the (Mg,Fe)O than the mechanism in Equation 4.5 would. However, given that we cannot distinguish $(Mg_{0.06}Fe_{0.94})O$ from FeO, if our buffered $(Mg_{0.06}Fe_{0.94})O$ were slightly enriched in Fe compared to the unbuffered $(Mg_{0.06}Fe_{0.94})O$, we would not know how to distinguish the two without sample recovery.

4.6 Rhombohedral Distortion of $(Mg_{0.06}Fe_{0.94})O$

Volumes and lattice parameters of rhombohedral-structured $(Mg_{0.06}Fe_{0.94})O$ were fit using methods described above. As depicted in Figure 4.2, rhombohedral $(Mg_{0.06}Fe_{0.94})O$ was stable at room temperature at pressures higher than 20 GPa. In the unbuffered experiment, room temperature patterns revealed a mixture of rhombohedral and cubic phases, while in the buffered experiment, only rhombohedrally-structured (Mg,Fe)O was present higher than 34 GPa.

Figure 4.8 shows the evolution of the lattice reflections of $(Mg_{0.06}Fe_{0.94})O$. Before-heating points, shown in gray, show the cubic (111), (200) and (220) reflections that split accordingly: $(111)_C \rightarrow (003)_R+(101)_R$ and $(220)_C \rightarrow (104)_R+(110)_R$. These five reflections were used to refine the unit cell volume. Black circles show measurements of the buffered dataset, and are less scattered than the white circles. Pressure was determined using the (111) and (200) reflections of solid neon (*Dewaele et al.*, 2008) or by the (100), (200), (101), (102), (110), (103), and (112) reflections of *hcp*-iron (*Dewaele et al.*, 2006).

Despite the obvious mismatch between the two datasets in the (003) reflection below 47 GPa, the two datasets appear to agree within scatter above 47 GPa. This observation is more apparent in Figure 4.9, which shows the c/a ratio of the hexagonal unit cell for each measurement. Above 55 GPa, the c/a ratios of the two datasets are indistinguishable. Another observation we note here is the leveling off of the distortion, apparently starting at 70 GPa.

This dataset shown in Figure 4.10, combined with the low-pressure measurements taken at Sector 3-ID-B (Section 3.4.1), was used to constrain the equation of state of $(Mg_{0.06}Fe_{0.94})O$ at 300 K for use in determining the pressure and sound velocities from NRIXS data (see 3.4.1).

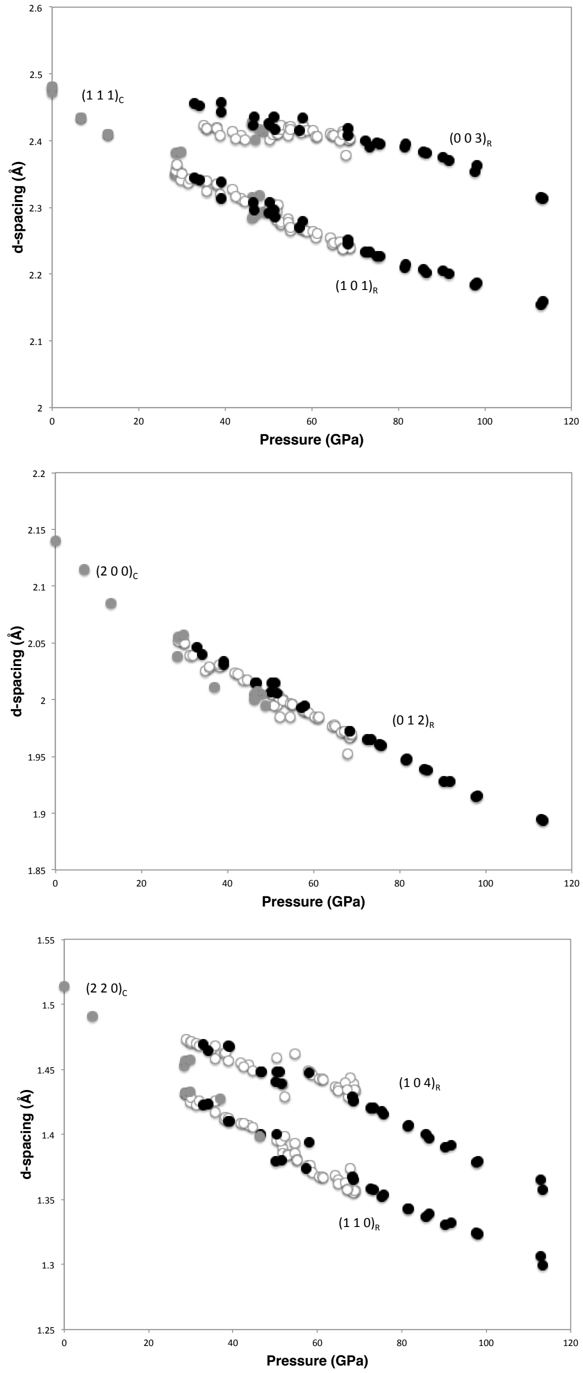

Figure 4.8: Evolution of *d*-spacings of $(Mg_{0.06}Fe_{0.94})O$ as a function of pressure. Gray circles: before heating experiment began. White circles: unbuffered dataset. Black circles: buffered dataset. Pressure was determined from the unit cell of neon (*Dewaele et al.*, 2008).

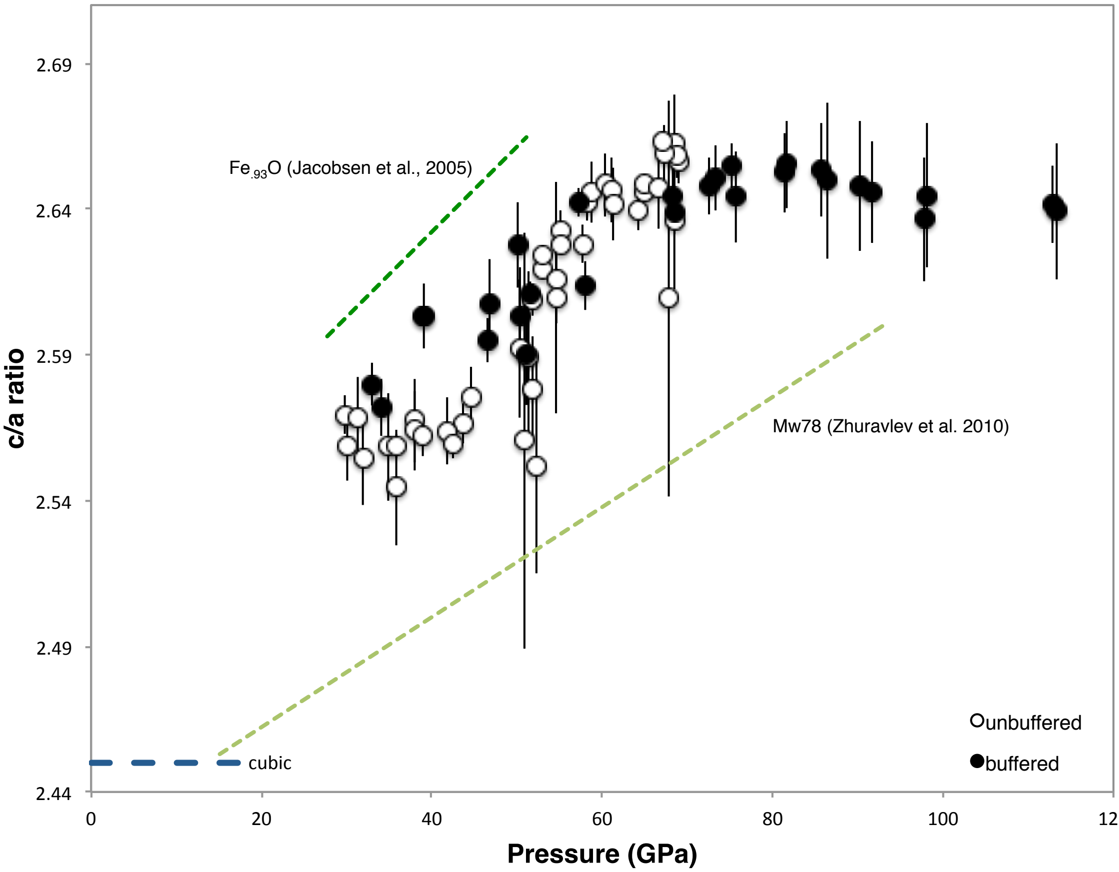

Figure 4.9: Evolution of c/a ratios of rhombohedral $(Mg_{0.06}Fe_{0.94})O$ as a function of pressure at 300 K. White circles: unbuffered dataset. Black circles: buffered dataset. Pressure was determined from the unit cell of neon (*Dewaele et al.*, 2008). Error bars are determined from the unit cell refinement.

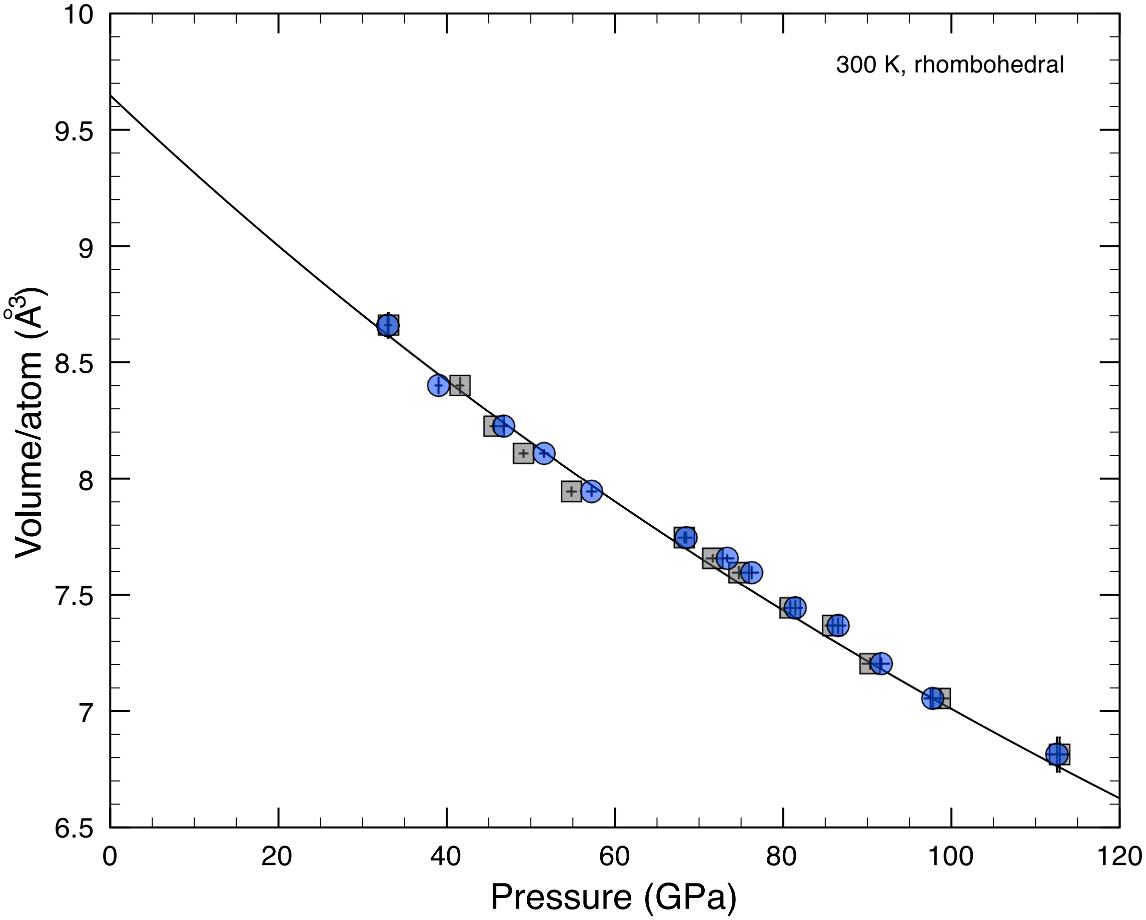

Figure 4.10: Pressure-volume data of quenched, rhombohedral ($Mg_{0.06}Fe_{0.94}$)O at 300 K, with pressure determined either by *hcp*-Fe (*Dewaele et al.*, 2006, gray squares) or Ne (*Dewaele et al.*, 2012, blue circles). Quench points are those after each heating cycle. Black line is a 3rd-order Vinet equation of state fit to the data using pressure determined from the equation of state of neon, where $V_0 = 9.65(7)$ Å^3/atom, $K_{0T} = 281(22)$ GPa, and $K'_{0T} = 0.6(4)$.

Table 4.6: Pressure-volume data for the buffered experiment at 300 K. [a]Pressure was determined from the equation of state of *hcp*-Fe (*Dewaele et al.*, 2006). [b]Pressure was determined from the equation of state of Ne (*Dewaele et al.*, 2008). [c]Volumes of *hcp*-Fe were refined using 7 reflections: (100),(200), (101), (102), (110), (103), and (112). [d]Volumes of Ne were determined using 2 to 3 reflections of (111), (200), and (220). [e]Measurements after each heating cycle is referred to in the text as "quench" points.

P_{Fe}[a] (GPa)	P_{Ne}[b] (GPa)	Vol_{Fe}[c] Å^3	Vol_{Ne}[d] Å^3	Vol_{Mw} Å^3/atom	a_{Mw} Å	c_{Mw} Å	Vol_{NaCl} Å^3
112.8(8)	113(1)	16.45(2)	25.39(7)	6.84(1)	2.612(7)	6.90(3)	20.10(4)
112.9(6)[e]	113.3(9)	16.45(1)	25.36(5)	6.81(5)	2.60(1)	6.87(5)	20.05(4)
98.3(5)	98(2)	16.84(2)	26.4(2)	7.10(5)	2.64(1)	6.99(5)	20.84(2)
98.7(4)[e]	98(3)	16.83(1)	26.4(2)	7.04(4)	2.65(1)	6.98(5)	20.78(2)
89.5(9)	90(2)	17.10(3)	26.9(1)	7.20(7)	2.66(1)	7.05(5)	21.42(9)
90.4(4)[e]	92(1)	17.08(1)	26.8(1)	7.20(6)	2.66(1)	7.04(4)	21.24(2)
85.1(3)	86(1)	17.24(1)	27.3(1)	7.31(5)	2.672(9)	7.09(4)	21.62(3)
85.8(2)[e]	86(2)	17.218(8)	27.2(1)	7.30(6)	2.67(2)	7.08(6)	21.53(2)
80.5(4)	82(1)	17.39(1)	27.66(9)	7.41(5)	2.683(8)	7.13(3)	21.92(3)
80.8(3)[e]	81(1)	17.38(1)	27.7(1)	7.39(4)	2.683(8)	7.12(3)	21.88(3)
74.0(4)	75(1)	17.62(2)	28.3(1)	7.56(3)	2.703(5)	7.17(2)	22.39(3)
74.7(4)[e]	75.8(6)	17.59(1)	28.21(6)	7.56(3)	2.704(6)	7.16(2)	22.31(2)
71.3(3)	73(1)	17.71(1)	28.5(1)	7.63(3)	2.712(8)	7.18(1)	22.62(2)
71.6(4)[e]	73.3(6)	17.70(1)	28.45(6)	7.62(3)	2.71(1)	7.18(2)	22.57(2)
67.9(7)	68(1)	17.84(3)	29.0(1)	7.78(4)	2.731(7)	7.22(2)	22.99(4)
68.3(4)[e]	68(1)	17.83(2)	29.0(1)	7.73(3)	2.727(5)	7.20(2)	22.87(2)
55.4(6)	58(1)	18.35(3)	30.2(1)	8.08(3)	2.777(6)	7.26(2)	23.9(1)
55(1)[e]	57(1)	18.38(5)	30.3(1)	7.94(2)	2.751(3)	7.27(1)	23.88(4)
48.6(6)	50.1(3)	18.66(3)	31.35(5)	8.18(6)	2.78(1)	7.32(3)	24.70(5)
49.1(8)[e]	51.5(2)	18.64(4)	31.12(3)	8.11(2)	2.781(4)	7.26(1)	24.58(3)
48.3(7)	46.5(3)	18.68(4)	31.93(5)	8.22(3)	2.800(6)	7.27(2)	25.15(2)
45.6(4)[e]	46.8(3)	18.81(2)	31.89(5)	8.17(6)	2.79(1)	7.27(3)	25.12(2)
38(1)	39(1)	19.23(4)	33.3(3)	8.47(4)	2.825(7)	7.35(3)	26.27(6)
39(1)[e]	40(1)	19.15(2)	33.2(2)	8.42(1)	2.819(2)	7.34(1)	26.13(2)
33(1)	34(2)	19.52(3)	34.5(4)	8.55(4)	2.845(6)	7.32(2)	26.8(1)
33.1(4)[e]	33(2)	19.50(2)	34.7(5)	8.58(3)	2.846(5)	7.34(2)	26.99(5)